Lidar and Triple-Wavelength Doppler Radar Measurements of the Melting Layer: A Revised Model for Dark- and Brightband Phenomena

KENNETH SASSEN, JAMES R. CAMPBELL, AND JIANG ZHU

Geophysical Institute, University of Alaska Fairbanks, Fairbanks, Alaska

PAVLOS KOLLIAS

Rosenstiel School of Marine and Atmospheric Science, University of Miami, Miami, Florida

MATTHEW SHUPE

NOAA/Environmental Technology Laboratory, Boulder, Colorado

CHRISTOPHER WILLIAMS

Cooperative Institute for Research in Environmental Sciences, University of Colorado, and NOAA Aeronomy Laboratory, Boulder, Colorado

ABSTRACT

During the recent Cirrus Regional Study of Tropical Anvils and Cirrus Layers (CRYSTAL) Florida Area Cirrus Experiment (FACE) field campaign in southern Florida, rain showers were probed by a 0.523-μm lidar and three (0.32-, 0.86-, and 10.6-cm wavelength) Doppler radars. The full repertoire of backscattering phenomena was observed in the melting region, that is, the various lidar and radar dark and bright bands. In contrast to the ubiquitous 10.6-cm (S band) radar bright band, only intermittent evidence is found at 0.86 cm (K band), and no clear examples of the radar bright band are seen at 0.32 cm (W band), because of the dominance of non-Rayleigh scattering effects. Analysis also reveals that the relatively inconspicuous W-band radar dark band is due to non-Rayleigh effects in large water-coated snowflakes that are high in the melting layer. The lidar dark band exclusively involves mixed-phase particles and is centered where the shrinking snowflakes collapse into raindrops—the point at which spherical particle backscattering mechanisms first come into prominence during snowflake melting. The traditional (S band) radar brightband peak occurs low in the melting region, just above the lidar dark-band minimum. This position is close to where the W-band reflectivities and Doppler velocities reach their plateaus but is well above the height at which the S-band Doppler velocities stop increasing. Thus, the classic radar bright band is dominated by Rayleigh dielectric scattering effects in the few largest melting snowflakes.

1. Introduction

Much of our planet's precipitation originates as snow far above the surface of the earth. Indeed, understanding the hydrological cycle requires a good working knowledge of the production of the ice particles that contribute to snow and rain under a variety of meteorological conditions. As a consequence of our knowledge of the physics of precipitation formation, snow and rain from melting snow are believed to be the dominant processes in temperate zones, and also probably play an important role in deep convective activity worldwide. Although the microphysical processes describing the transition of snowflakes to raindrops are by now well understood, the corresponding effects on the propagation of laser light and microwaves would appear to require more research. Now that precipitating clouds are coming under scrutiny from earth-orbiting radar systems (Simpson et al. 1996; Stephens et al. 2002), improving our understanding of the scattering and attenuation of microwaves in the melting layer is particularly warranted.

The most widely recognized remote sensing feature observed during the melting of snowflakes is the radar bright band. Named after the appearance of the narrow layer of strong signals on the oscilloscope displays of World War II vintage radars, it was not long before the

Corresponding author address: Kenneth Sassen, 903 Koyukuk Drive, Geophysical Institute, University of Alaska Fairbanks, Fairbanks, AK 99775.
Email: ksassen@gi.alaska.edu

main causes of the bright band were identified (for reviews see Battan 1973; Dennis and Hitchfield 1990). Because of the differences in the dielectric constants between water and ice, ice particles produce much weaker backscattering and attenuation in the Rayleigh scattering regime, such that radar returns in the rain are strongly enhanced, despite the larger sizes of the low-density (ice-plus-air mixture) snowflakes (Meneghini and Liao 2000), and the fact that the concentration of raindrops declines significantly because their fall speeds are much greater than the snowflakes from which they are derived.

A major factor contributing to the radar bright band is a consequence of the manner in which snowflakes melt—the ice surfaces become coated with liquid, accumulating to a sufficient depth to scatter essentially like equivalently sized water particles. These wet snowflakes are nonspherical and still relatively large, which, in combination, generates strong microwave backscattering. At millimeter wavelengths a brightband effect is typically absent, and a radar dark band has even been reported for W-band radars near the expected brightband position (Lhermitte 1988). Other factors that have been considered involve the aggregation/coalescence or breakup of snowflakes and raindrops, which, because of the diameter-to-the-sixth (D^6) power law of Rayleigh scattering, can have noticeable effects on radar signals. However, as pointed out by L. J. Battan (1978, personal communication), any radar brightband theory that *relies* on particle aggregation or breakup is not likely to succeed universally. Interestingly, there is an analog of the bright band with lidar, but the lidar bright band owes its existence to the increasingly strong snowflake backscattering with height coupled with the overwhelming attenuation rate in the snowfall surrounding the freezing level, which creates a feature resembling a bright band on an oscilloscope display (Sassen 1977a).

The lidar dark band, on the other hand, is a recently recognized curiosity of melting-layer remote sensing. Although long serendipitously captured in lidar returns from precipitation, its meaning and significance were concealed essentially because of a lack of prolonged data collection in rainfall; lidar systems needed to be shielded from precipitation, and other (optically less dense) targets were favored. It was not until relatively recently that Sassen and Chen (1995) comprehensively studied this phenomenon and gave it a name. More recent observations have been reported in Demoz et al. (2000) and Roy and Bissonnette (2001). The term lidar dark band, in contrast to the radar bright band, delineates its quintessential property. It is a backscatter intensity minimum that occurs surprisingly not far in height from the location of the radar bright band. Based on an analysis of coordinated aircraft, polarization lidar, and W-band (0.32 cm) Doppler radar measurements, it was concluded by Sassen and Chen (1995) that this "remarkably narrow and consistent feature" corresponds to a stage of snowflake melting that produced "inhomogeneous ice-containing raindrops formed by the structural collapse of severely melted snowflakes." It occurs because of the cross-sectional area-dependent differences (i.e., D^2) in lidar backscattering between near-spherical raindrops and the much larger snowflakes aloft.

Unfortunately, it has yet to be determined how representative the Sassen and Chen (1995) findings are, particularly with regard to the melting-layer temperature structure, the precipitation rate and mechanism, and how measurements at other radar wavelengths compare. The same can be said of the representativeness of the available W-band radar dark-band case studies. We begin addressing these issues in the current study based on a unique ensemble of remote sensors.

2. The dataset

The National Aeronautics and Space Administration (NASA) Cirrus Regional Study of Tropical Anvils and Cirrus Layers (CRYSTAL) Florida Area Cirrus Experiment (FACE) field campaign, carried out during July 2002 in the southern Florida region, was designed to research subtropical thunderstorms and the cirrus clouds derived from their anvils. In addition to six project aircraft, three surface sites were equipped with various arrays of remote sensing systems to obtain more continuous atmospheric observations and serve as hubs for the aircraft operations. The eastern site at the Kendall-Tamiami Executive Airport (~25 km southwest of Miami) was uniquely equipped with three Doppler radars and a radiation measurement suite that included a near-continuously operated eye-safe lidar (see Table 1 for remote sensor specifications). Data were also collected by a Joss–Waldvogel disdrometer located at this site to obtain high (1 min)-resolution rainfall-rate measurements (Joss and Waldvogel 1990). It should be noted, however, that rain measurements at the surface can differ greatly from conditions aloft in the melting region (~3.5–4.5 km above sea level, in our case) because of temporal variations in the convective showers. Figure 1 shows an aerial photograph of the instruments deployed at the field site.

The micropulse (0.523 μm) lidar (MPL; Spinhirne 1993) is a compact, eye-safe device, which is being increasingly utilized worldwide at ground-based observing sites for unattended cloud and aerosol observations. Eye safety is achieved by using a rapidly pulsed (2.5 KHz), low-powered (1.0 W) laser source that is expanded through a transmit–receive Cassegrain telescope. This feature allows the instrument to be operated full time in an autonomous fashion. (At CRYSTAL FACE, however, data collection was typically suspended around solar noon—the *lidar siesta time* of the Tropics—because of the excessive ambient solar background that adversely affected the photon-counting detector.) Campbell et al. (2002) have recently described the instrument in detail and summarized the relevant MPL data processing techniques.

TABLE 1. Specifications of the MPL and the three radars deployed at the eastern CRYSTAL FACE field site. The differences exemplify the wavelength-dependent range of operational characteristics of modern remote sensors.

	MPL	W band	K band	S band
Wavelength	0.523 μm	0.32 cm	0.86 cm	10.6 cm
Peak power (W)	1.0	1000	100	500
Maximum PRF (KHz)	2.5	10	7.7	8.0
Pulse width	10 ns	0.2 μs	0.3 μs	0.4 μs
Beamwidth	50 μrad	0.24°	0.3°	3.0°
Receiver diameter (m)	0.2	0.9	1.8	3.0
Receiver gain (dBZ)	—	58	165	—
Range resolution (m)	75	30	45–90	60
Time resolution (s)	60	60	9–35	10
Range gates	800	512	184	244
Sensitivity at 5.0 km	—	−37 dBZ	−28 dBZ	−6 dBZ
V resolution (cm s^{-1})	—	3.2	6.4	13.9

The three participating zenith-pointing Doppler radar systems represent a unique combination of millimeter-wave to microwave sensors (see Table 1). Atmospheric probing at the shortest 0.32-cm (94-GHz frequency) wavelength of W-band radars is sensitive to relatively small cloud droplets and ice crystals, although pulse attenuation in rain and melting snow can have noticeable effects on the returned signals. The University of Miami 94-GHz Doppler Cloud Radar (UMDCR; Albrecht et al. 1999) is a single-antenna version of the radar developed during the early 1980s (Lhermitte 1988). The lightweight UMDCR uses a high pulse repetition frequency that yields a Doppler velocity window of ±8 m s^{-1} at high spatial and temporal resolutions (typically 30 m in height by 1 s, respectively). With an antenna beamwidth of 0.24°, the radar horizontal sample size is about 20 m at 5 km. High-FFT-resolution Doppler spectra are provided by a real-time FFT algorithm (256, 512, or 1024 FFT points) at all range gates sampled by the processor. This gives excellent Doppler spectra resolution (Table 1).

At the somewhat longer 0.86-cm wavelength (34.86-GHz frequency) K$_a$-band wavelength, the National Oceanic and Atmospheric Administration (NOAA) millimeter cloud radar (MMCR; Moran et al. 1998) shares many of the capabilities of the W-band radar, but with reduced attenuation effects. The MMCR provides continuous profiles of the equivalent radar reflectivity factor Z_e (mm^6 m^{-3}) and the Doppler spectrum through clouds and precipitation with approximately 10-s temporal and 45–90-m vertical resolutions, using 128 FFT points. Despite a low-peak-transmitted power of 100 W, the MMCR achieves high sensitivity using a large antenna, long sampling times, and pulse compression techniques (Moran et al. 1998).

In contrast to the millimeter-wave radars, the NOAA 10.6-cm (2.835-GHz frequency) S-band radar cannot generally observe the particles suspended in a cloud, but rather observes the larger particles that are precipitating out of a cloud. Such radars are *traditional* in the sense that pulse attenuation is rarely significant and the returned radar signals can be treated relatively simply

with the Rayleigh scattering theory. This vertically pointing profiler (Ecklund et al. 1999) uses a 3-m parabolic dish antenna and a peak power of 500 W to observe the precipitating particles while they advect overhead. This unit was operated with a 10-s temporal and a 60-m vertical resolution, and alternated between an uncoded and a 10-bit-coded pulse compression mode.

During the early part of the CRYSTAL FACE campaign of interest here, a broadening area of low pressure developed in the south-central Gulf of Mexico, yielding easterly to southeasterly low-level flow over the research area. In contrast to the usual strong diurnal convective activity expected during midsummer months (Michaels 1985), rainfall at this time was often more continuous in nature. While not inhibiting strong convective cell development, more stratiform rainfall events were also encountered. Such conditions are more amenable for observing radar/lidar melting-layer

FIG. 1. Aerial photograph of the eastern CRYSTAL FACE field site at the Kendall-Tamiami Executive Airport near Miami, where (clockwise from the top right of the tarmac) the roof-mounted NOAA K-band Doppler radar, the NASA Surface Measurements for Atmospheric Radiative Transfer (SMART) van that held the MPL and several radiometers, the circular rain guard enclosing the NOAA S-band radar dish, and the free-standing University of Miami W-band Doppler radar attached to its supporting van are shown.

phenomena than in strong thunderstorms, with their intense vertical motions and highly variable precipitation conditions.

3. Data and analysis

Prior to showing examples from the multiple remote sensor dataset, it is useful to overview the scattering conditions to be expected at each wavelength in the melting layer, where various Rayleigh and non-Rayleigh effects will be manifested. Lidar scattering can be described by the principles of geometric optics, where the D^2 law and the precise shape of the ice, mixed-phase, and water particles govern the backscattering behavior, and the attenuation of the laser pulse will generally be significant. For an S-band radar, it can be assumed that Rayleigh scattering dominates under these conditions, such that hydrometeor scattering can be treated with spherical and spheroidal dipole particle models, and is governed by the D^6 power law and the hydrometeor refractive index (i.e., phase), while attenuation is unimportant. This corresponds to the traditional radar brightband scenario.

However, at the millimeter W- and K-band radar wavelengths, a mixture of Rayleigh and non-Rayleigh scattering effects will come into play. We show in Fig. 2 how the normalized radar backscattering cross sections for spherical water drops depend on the radar wave-
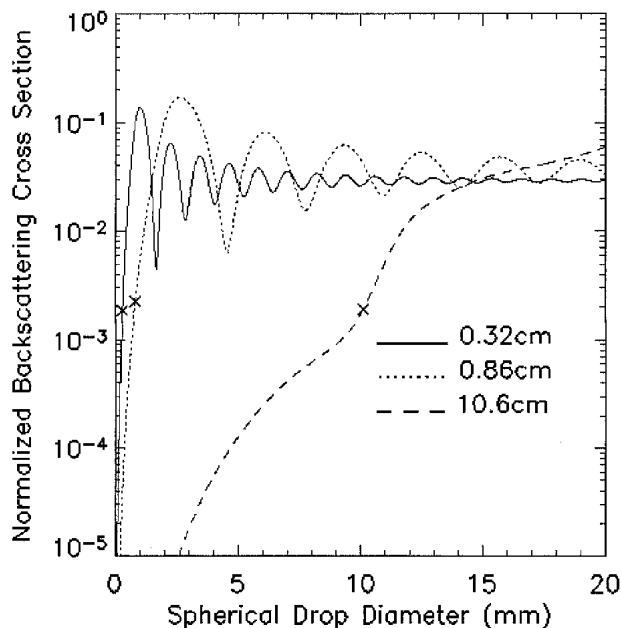

FIG. 2. Comparison of normalized backscattering cross sections (i.e., backscatter coefficients divided by particle cross-sectional areas) vs spherical water drop diameter for the three indicated radar wavelengths, showing how Mie scattering effects emerge at different drop sizes as a function of wavelength. The "x" symbols define the general upper limit for Rayleigh backscattering by spheres.

length λ. The two scattering domains are clearly revealed by the slope changes in the curves. For relatively small spheres, the steep slopes delineate the D^6 Rayleigh domain, while horizontal lines (i.e., backscattering normalized by dividing by D^2) define the geometrical optics domain that requires the use of the intensive Mie computations. In between the two limits is a transition zone often marked by large oscillations caused by backscattering resonances. The "x" symbols locate the usual upper limit for Rayleigh scattering as expressed in terms of the size parameter $\chi = \pi D / \lambda$, which is $\chi \approx 0.3$ for spheres (Kerker 1969). Clearly, interpreting melting-layer observations at millimeter wavelengths present greater challenges in comparison to the relative simplicity of the traditional radar Rayleigh theory for S-band radars.

An example of the appearance of the various melting-layer backscattering phenomena observed by the four active remote sensors over a 5-h period on 8 July is given in the height-versus-time displays in Fig. 3, where the sensor wavelength decreases from top to bottom. Note that a colored radar reflectivity scale (in decibels, 10 times log mm^6 m^{-3}) is given to the right of each radar display, and that the range-normalized attenuated lidar backscattering (in arbitrary units) is also based on a logarithmic scale. Over this period, rain showers of various intensities occurred (see the bottom panel for surface disdrometer rainfall rate data). The S-band radar display at the top shows a consistent radar bright band centered at ~4.3 km height above mean sea level (MSL), whose intensity tends to vary with the rainfall rate. The K-band radar display sometimes indicates a comparatively weak bright band at a similar height, but only under weakly precipitating conditions. Although no evidence for a bright band is apparent in the W-band radar display, a weak radar dark band is indicated by a decline in radar signals at ~4.5 km MSL from 1430 to 1500 UTC, where dBZ are, in contrast, increasing slightly at the other radar wavelengths (see below).

The lidar display is quite dissimilar because of the dominating effects of optical attenuation by hydrometeors, especially in the occasional water clouds below 1.0 km and from ~3.0 to 4.0 km MSL early on and in the middle of the period. Lidar dark bands are easily seen centered just above 4.0 km from ~1350 to 1440 and 1615 to 1720 UTC, which corresponds to periods when the lidar pulse was able to penetrate high enough to sample the snow causing the rain. Note that the rapid signal decrease with height in the snow aloft is due to overwhelming attenuation, which is verified by the radar data, indicating much higher cloud-top heights, and produces a lidar bright band at ~4.5 km. It is also interesting to note the differences in the cloud-top heights sensed by the radars, which reflect the effects caused by variable wavelength-dependent attenuation rates versus the λ^{-4} sensitivity to particle size that favors ice cloud detection by millimeter-wave radars, as
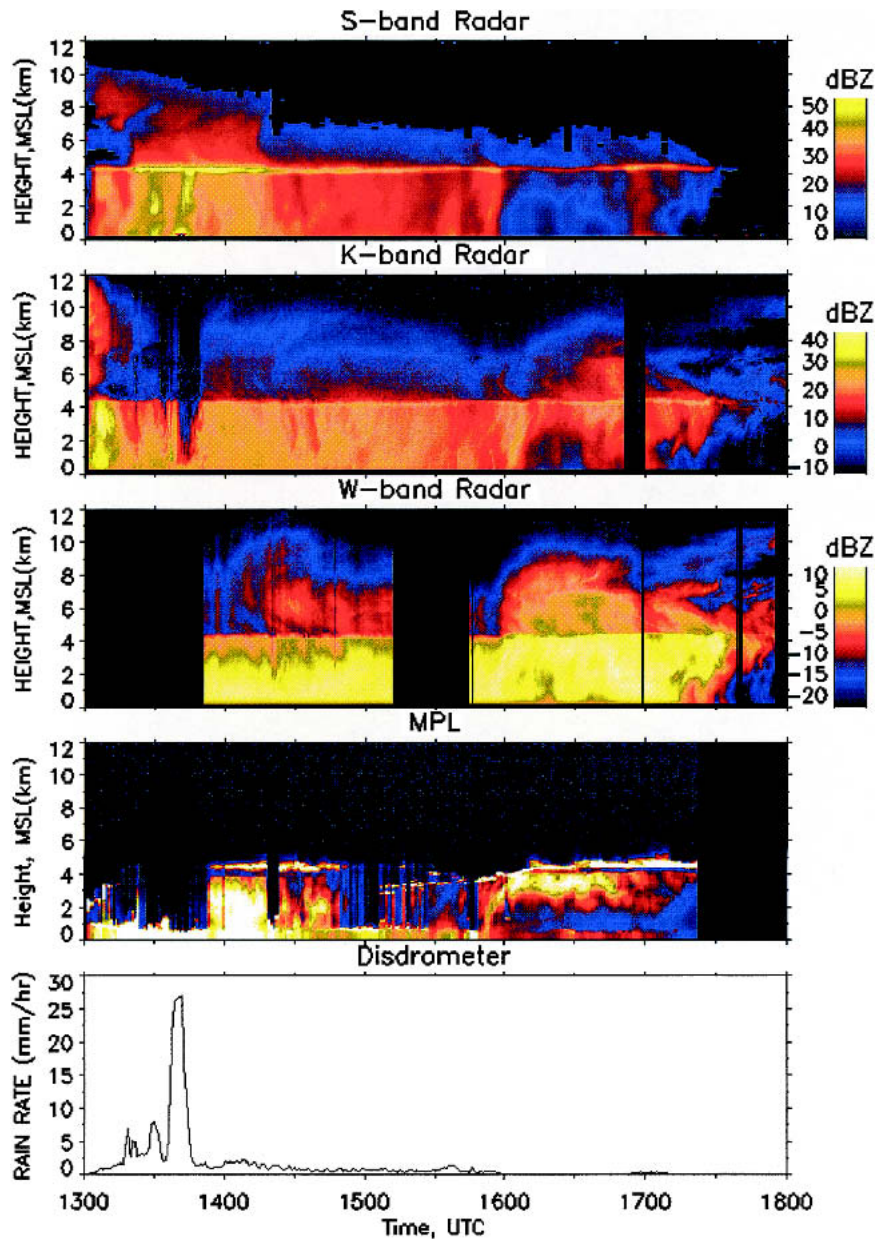
FIG. 3. Comparison of returned laser energy and triple radar reflectivity factor Z_e height vs time displays over the 1300–1800 UTC period on 8 Jul 2002, during a series of rain showers. Gaps in the data records are present for all but the S-band system. Note that the radar Z_e values have been affected by wavelength-dependent backscattering and attenuation effects and system calibration uncertainties. (bottom) The surface rainfall rate measured by the disdrometer.

well as basic sensor sensitivities (Table 1). Note that although the K-band radar in this case had a faulty preamplifier, which the reduced signal levels by ~20 dBZ, the ice cloud–top heights are higher than at 10.6 cm in the absence of strong rainfall-induced attenuation. Particularly near the end of the period, the W-band radar senses more of the nonprecipitating clouds present due to the λ^{-4} Rayleigh law. These melting-

layer features are examined in greater detail below for this and an additional case study.

Compared in Figs. 4a–c are 10-min-averaged MPL and Doppler radar profiles for three periods on the indicated days, showing obvious lidar dark bands. The closest Miami radiosonde temperature profiles are given at the right (the location of 0°C is highlighted), but it should be acknowledged that the precipitation
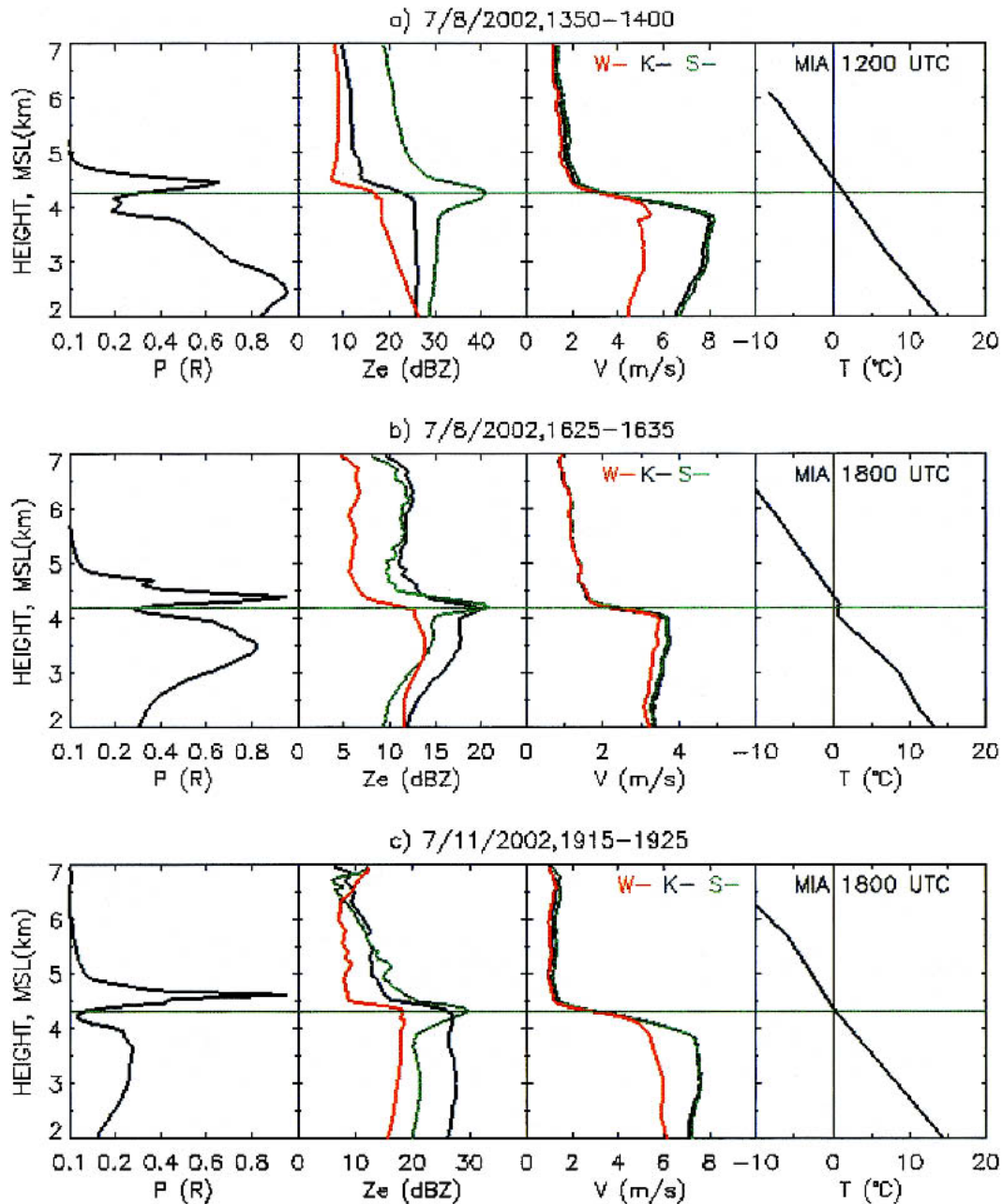
FIG. 4. From left to right, 10-min-averaged vertical profiles of relative returned laser power $P(R)$ from the MPL, equivalent radar reflectivity factor Z_e (dBZ) and mean Doppler velocity V for the three radars (see inserted color key), and temperature profile from the closest Miami (MIA) radiosonde for (a) 1350–1400 UTC 8 Jul, (b) 1625–1635 UTC 8 Jul, and (c) 1915–1925 UTC 11 Jul 2002. The horizontal green line gives the height of the maximum S-band radar brightband signal. In (a), the range of radar reflectivities has been compressed by adding 22 and 5 dBZ to the W- and K-band data, respectively. (This signal manipulation is warranted in view of radar Z_e uncertainties caused by non-Rayleigh scattering effects and attenuation, and also to some extent by radar calibration and sampling issues.) In (b) 8 dBZ and in (c) 13 dBZ were added to the W-band radar Z_e.

process can significantly alter the local atmospheric structure (Stewart et al. 1984) and make routine (12 hourly) sounding data unrepresentative. (For example, note the presence of the isothermal layer in Fig. 4b, which is likely caused by the cooling effect of melting

snowflakes near Miami at that time.) The data quantities are attenuated returned power for lidar (in arbitrary units), Z_e, and mean Doppler velocity V for the three radars. Note that the radar dBZ scale is valid in each case for the S-band data, with the W- and K-band

profiles often adjusted to compress the dynamic range of the total signals and to facilitate the data intercomparison (see figure caption). As indicated in Fig. 3, millimeter-wave radar returns are often much weaker because their radar pulse attenuation rates are significantly higher in the rain and melting zones. Radar calibrations issues and pointing uncertainties may also have had an effect. Thus, we are more interested in the relative variations in the radar signals than their absolute magnitudes. The profiles from 2.0 to 7.0 km MSL bracket the melting layer, and shown for reference as the horizontal green lines are the heights of the maximum S-band brightband signals.

Figure 4a provides a case from the morning of 8 July corresponding to a moderate rain shower; the corresponding 10-min-averaged surface rainfall rate measured by the disdrometer (Fig. 3) was only 1.52 mm h^{-1}, however. Strong optical attenuation is apparent in the rain and snow, which contributes to a relatively narrow lidar bright band centered near the 0°C isotherm. The lidar dark band is broad with two signal minima. The radar profiles show large Z_e increases from the top to the bottom of the melting layer, but the details differ significantly with wavelength. A relatively weak W-band radar dark band of ~3 dBZ occurs at the top of the melting zone at 4.5 km (a ~6 dBZ decrease is found in the example given by Lhermitte 2002), while a bright band is clearly present in the S-band radar data at 4.25 km. The absence of W- and K-band bright bands indicates that Rayleigh scattering conditions in the melting snow were violated at these wavelengths. The Doppler mean velocities also show a steady increase descending through the melting layer. However, although the Vs are similar at ~1.5 m s^{-1} in the snowfall, the W-band fall speeds abruptly stop increasing at ~4.5 m s^{-1}, which is also due to non-Rayleigh effects. That is, the K- and S-band radar Doppler V data are weighted toward the largest, fastest-falling raindrops, which are too large at the 0.32-cm wavelength to behave as Rayleigh scatterers, and so have a lessened impact on the mean weighted V. The unusual occurrence of the dual minima in the lidar dark band is probably a result of the presence of a mixture of ice particle fall streaks with different size or type characteristics, which can lead to multiple radar bright bands (Fabry and Zawadski 1995). Note the corresponding kink in the W-band radar V profile in the lower melting layer, which is also indicative of a mixture of hydrometer types.

The two cases in Figs. 4b,c are from light intensity rain showers on the afternoon of 8 and 11 July (0.07 and 0.09 mm h^{-1} at the ground, respectively), under which conditions the lidar signals are obtained from greater heights above the strongly peaked lidar bright bands, owing to smaller attenuation rates. The lidar and radar signals increase in the rain with height in Fig. 4b, indicating that the rain shower was in the process of descending or that raindrop evaporation was occurring. The lidar dark bands are rather symmetrical and cen-

tered ~100 m below the peaks in the S-band radar bright bands in both cases. In Fig. 4b, a K-band radar bright band is clearly indicated, with a peak slightly below the S-band radar brightband center. Furthermore, all three Doppler radar V profiles are in reasonable agreement, peaking at ~3.5 m s^{-1}. In other words, the particle sizes in the very light rain in this case did not significantly exceed the Rayleigh limit: the disdrometer data show that few drops exceeded a 1.0-mm diameter.

As in the first example, the data in Fig. 4c show wavelength-dependent Doppler velocity differences and the absence of radar bright bands in both the W and K bands. Doppler V are, interestingly, quite similar at the K- and S-band wavelengths. In other words, the absence of a K-band radar bright band indicates that the larger melting, *nonspherical* particles violated the Rayleigh scattering assumption, unlike the raindrops derived from them. The W-band radar signals are rather constant above the melting zone, in contrast to the gradually increasing Z_e at the other wavelengths. Because signal increases approaching the melting level from above are typically attributed to ice crystal aggregation, W-band radar dark-band effects may have counteracted this tendency in this case.

4. Discussion

The interrelationships between the various optical and microwave melting-layer features illustrated by the characteristic profiles in Fig. 4 lead us to the conceptual wavelength-dependent model given in Fig. 5. Here we use basic hydrometeor models to help explain the backscattering phenomena as low-density snowflakes (i.e., dendritic ice crystal aggregates) transit into homogeneous near-spherical raindrops (as in Mitra et al. 1990). Effects caused by particle coagulation or breakup are ignored. Although we show the position of the 0°C isotherm for reference, the temperature gradient in the melting layer may be highly variable because of evaporative cooling, vertical motion, and other factors, so we choose not to provide a vertical temperature or height scale. It should also be kept in mind that the exact nature of the ice particles undergoing the phase change, including their density, size distribution, and amount of riming, will affect the backscattering and velocity outcomes within the melting layer.

At the left-hand side in Fig. 5 is schematically illustrated the hydrometer type as follows: (starting from the top) a dry snowflake, two melting snowflake models in which water coatings are accumulating on the ice crystal branches and interbranch cavities of the shrinking particles, an irregular water-enclosed severely melted snowflake, a near-spherical mixed-phase drop, a drop with most of the ice melted, and, finally, a homogeneous raindrop. The relative size of the particles is based roughly on a 10:1 ice-to-water particle density
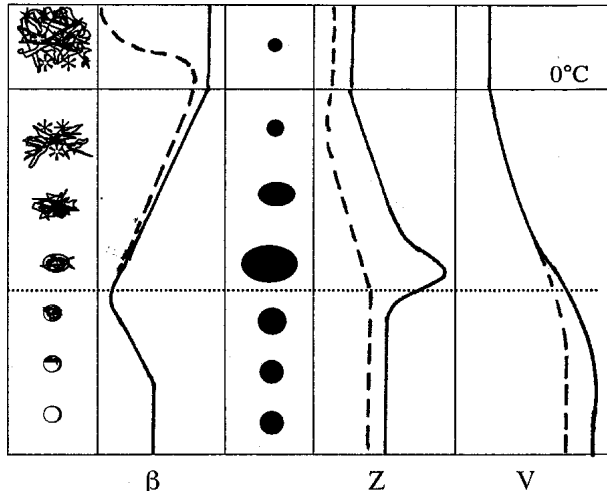
FIG. 5. A schematic representation of the hydrometeor shapes responsible for the various lidar and radar bright- and dark-band features of the melting layer. At left are detailed models of melting dendritic snowflakes (i.e., from top to bottom) that visible wavelength lidars would sense and the corresponding lidar backscatter coefficients (β), with the effects of laser pulse attenuation shown by the dashed line. In the middle is a representation of the corresponding models that an S-band radar would sense. At right are idealized vertical profiles of radar Z_e and V for W- (dashed) and S-band (solid) radar. The relative position of the 0°C isotherm is shown for reference, and the horizontal dotted line corresponds to the lidar dark-band signal minimum.

ratio. These images are more or less what are actually sensed by visible wavelength lidar, where backscattering responds to the exact details of particle shape. In contrast, further to the right is a characterization of the radar cross sections that an S-band radar would sense, where simple particle models can be employed and the difference in particle phase (i.e., dielectric constant) is of significance to backscattering. Such Rayleigh scattering particle models are apparently always violated by the larger particles present in rain showers with W-band radars, such that a mixture of the optical and microwave models is, in effect, sensed. Accordingly, K-band radars, with their intermediate wavelengths, may sense conditions somewhere between the S and W bands, depending on the sizes of the hydrometeors in each case. The remainder of Fig. 5 shows idealized lidar backscattering (with the generic effects of attenuation on returned power above the dark band, included as the dashed line), and W- and S-band Z_e and V profiles.

First, it should be noted that the strong optical attenuation from the comparatively large (unmelted) snowflakes in the vicinity of the freezing level helps to create a lidar bright band whose characteristics depend on the precipitation rate. Radar reflectivities and mean fall speeds are constant in this region in the absence of aggregation. As snowflakes progressively melt below the 0°C isotherm and shrink in size, the laser backscattering cross sections steadily decrease, while the radar Z_e increases because of the increasing liquid water con-

tent (i.e., dielectric effect). The lidar signals reach a minimum at a stage of snowflake melting corresponding to a position just below the S-band radar brightband peak and even closer to the signal plateau in W-band radar Z_e. This leads us to reason that the lidar signals start to increase below the dark-band center because the wet snowflakes have collapsed into mixed-phase raindrops that can now benefit from spherical particle backscattering mechanisms, namely, surface waves and the front-face axial reflection. (This collapse happens when the surface tension of the accumulating liquid overwhelms the structural strength of weakened crystal branches.) The lidar signal increase below the dark-band center is aided by the removal from the drops center of the embedded ice mass due to final melting and/or internal drop circulations (Pruppacher and Beard 1970). This allows the final spherical particle contribution, the paraxial reflection off the far drop face, to come into play (Ro et al. 1968).

A comparatively small W-band radar Z_e decrease occurs high in the melting region under some conditions, corresponding to the position where mean Doppler V are just beginning to increase at all wavelengths (Fig. 4a). Thus, the W-band radar dark band is produced by large (non-Rayleigh) snowflakes that are just beginning to melt. As shown theoretically by Battan (1973) for large melting hailstones, a water coating on large ice particles can generate a decrease in radar backscattering because of the differences in the water and ice dielectric constants and the emergence of Mie scattering effects. This is shown in Fig. 6 in terms of Mie theory backscattering predictions for water and ice spheres tai-
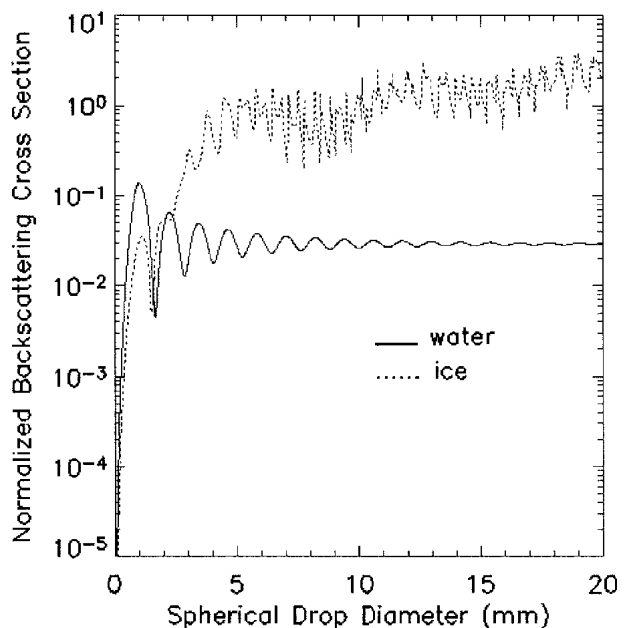

FIG. 6. A comparison of normalized backscattering cross sections for water and ice spheres calculated from Mie theory using the refractive indices for W-band radar.

lored to the W-band radar wavelength. It is clear that as particle sizes increase beyond the Rayleigh and transition zones, ice particles become considerably stronger backscatterers. Actually, once outside the Rayleigh domain, water absorbs the incident radiation so strongly that even microscopic coatings will reduce the backscattering from the underlying ice surfaces.

We hypothesize that an analogous situation occurs for snowflakes first entering above-freezing air. Namely, the external ice crystal branches melt first and acquire a thin water coating, which in later stages of melting will tend to accumulate and, by capillary action, gather in the interior of the particle. Although this exact microphysical model cannot presently be treated for melting snowflakes with sizes in the geometrical optics scattering regime, we provide in Fig. 7 the results of concentric ice/water sphere Mie backscattering simulations for melting particles of a constant size, using the Bohren and Huffman (1998) coated-sphere code and the W-band radar ice/water refractive indices given in Sassen and Liao (1996). Normalized backscattering cross sections are given for particles spanning the Rayleigh and Mie domains (see inserted total particle diameters).

The Rayleigh trending data (green lines) in Fig. 7 display D^6 dependence when in both the nearly pure ice (left axis) and pure water (right end of each curve) phases. Note the significant increase in backscattering during the ice-to-water phase change for the green curves, which illustrates one of the main causes of the radar bright band—the changeover in dielectric constants (Di Girolamo et al. 2003). Although the resonant backscattering behavior of the somewhat larger particles in the Rayleigh–Mie transition zone is complex, it is apparent that a strong decrease in W-band radar Z_e tends to occur for melting ice spheres in the Mie domain (gray curves), and the water thicknesses of the coatings are quite small. For many of the particles that show this effect in the ~2.0–5.0-mm diameter range, water coatings of only ~10–50 μm are apparently needed. When a size distribution of melting particles is present, it can be appreciated that a backscattering *well* would occur early during melting in the region where backscattering from large particles is decreasing, but just prior to the Rayleigh-induced particle scattering increases contributed by smaller particles. The minima in backscattering caused by resonances also tend to occur with similar water coatings. Although we acknowledge that this particle model is more applicable to melting sleet than low-density snowflakes, it should provide
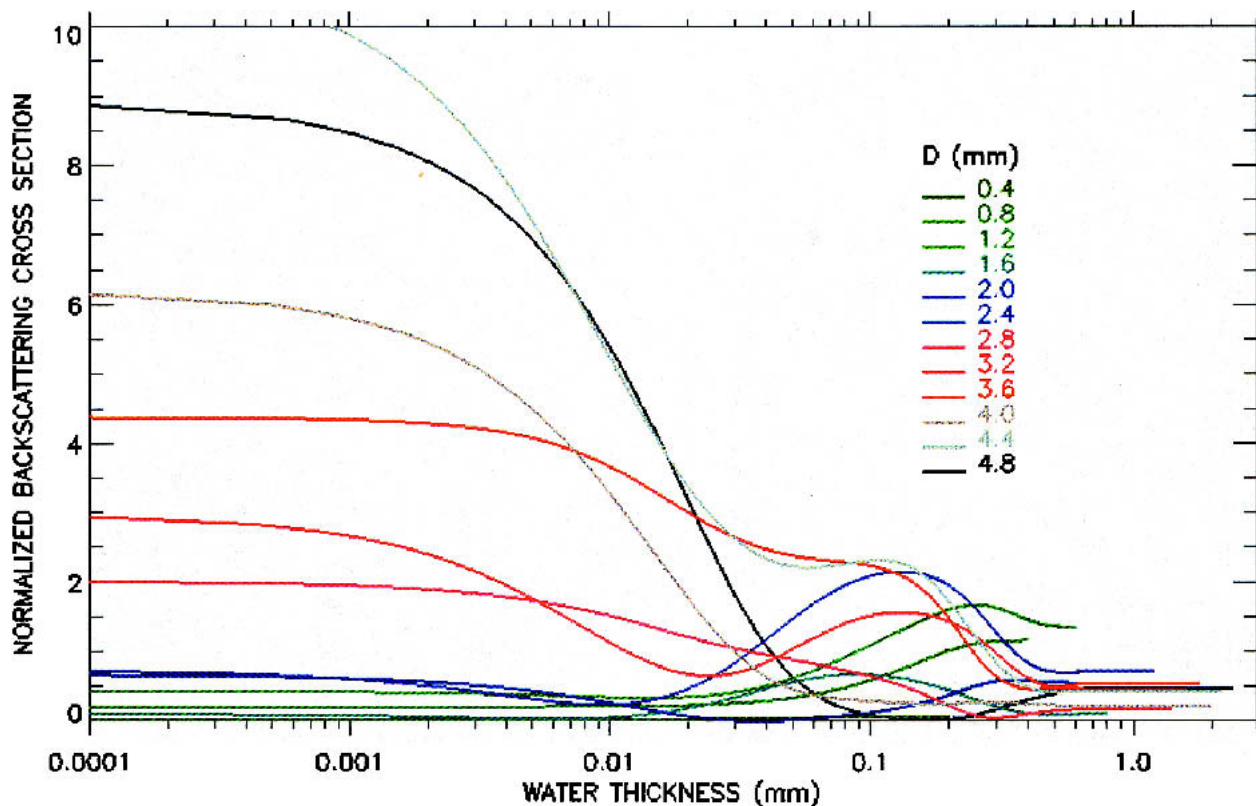

FIG. 7. Results of Mie theory for the normalized backscattering cross sections of concentric ice/water spheres for the indicated (constant) particle diameters D, aiding in the understanding of the *initial* behavior of melting snowflakes believed to be responsible for the W-band radar dark band. As non-Rayleigh scattering effects come into prominence ($D \sim > 1.0$ mm), the normalized radar backscattering cross sections tends to minimize with water coatings on the order of 10–50 μm.

insights into the effects of the initiation of the melting process on the W-band radar dark band.

The idealized vertical V profiles in Fig. 5 reinforce these inferences, although at first glance the S-band data would seem to indicate otherwise. Such traditional Doppler radar data show that particle fall speeds continue to increase to near the bottoms of the radar bright bands and lidar dark bands. However, this position is much lower than the usual positions of the W-band radar reflectivity plateaus, which must more accurately demarcate the *mean* position of the final snowflake-to-raindrop transition. The W-band Doppler V profiles in Figs. 4a and 4c, for example, show that V levels off at a higher relative position in the melting layer, which also tends to correspond to the millimeter-wave signal plateaus and the lidar dark-band center, than that position in S-band profiles. Thus, because the mean Doppler velocities in the Rayleigh domain are weighed according to the D^6 power law, S-band microwave radar data are strongly biased toward the few largest particles, which have fallen the fastest and melted the least.

5. Conclusions

In this study we intended to examine the nature of the lidar dark band using coordinated Doppler radar measurements in the melting region at three wavelengths, spanning the micro- to millimeter-wave regions (10.6–0.32 cm). Presumably, the radar backscattering features are better understood, and should, therefore, aid in explaining the lidar dark band. However, the microphysical/backscattering model that has resulted differs from previous models in some respects in both the optical and microwave domains. Unfortunately, as unique as this dataset is, lidar and radar depolarization data, which would have provided further information on the state of the melting particles, are not available from the instruments deployed at the eastern CRYSTAL FACE field site.

Prior to this study much of what was known of the lidar dark band was restricted to a single comprehensive case study that established its relation to W-band Doppler radar data and suggested a likely cause for this melting-layer feature (Sassen and Chen 1995). Our results confirm that mixed-phase particles are indeed involved in both the creation and destruction of the lidar dark band, with the initial laser signal increase resulting from the emergence of major spherical particle backscattering mechanisms immediately after the structural collapse of snowflakes, which is then followed by the melting of the embedded ice to finally disclose the drop center to backscattering. The presence and relative location of the triple-wavelength radar melting-layer phenomena here has been crucial in this assessment. The previous lidar dark-band model developed in Sassen and Chen (1995) involves the same basic scenario, but overemphasizes the contributions of the rear axial

backscattering component. Although in laboratory experiments using frozen pendent drops the particles backscattered ~1.5–5.0 times more energy after the central ice mass floated to the top of the drop (Sassen 1977b), lidar dark bands in the field can have more significant overall signal increases. The pendent particle shape and experimental setup (using a horizontally incident laser beam) does not provide a good model for melting snowflakes studied by zenith lidar. Moreover, the extent that nonspherical mixed-phase raindrop fall orientation affects the lidar melting-layer phenomena remains to be determined. Strong lidar backscattering anisotropy from aerodynamically distorted raindrops has recently been reported using a scanning lidar (Roy and Bissonnette 2001).

Comparison of the triple-radar returns in the bright-band region reveals significant wavelength-dependent Z_e differences, as well as differences in the basic Doppler signatures. Because the Doppler V from the three radars are weighted toward different portions of the particle size distribution, the positions of the snowflake-to-raindrop transition (i.e., the snowflake structural collapse) differ. The W-band radar measurements consistently failed to detect the strong backscatter enhancement that we refer to as the radar bright band, and only noted a gradual Z_e increase due to the refractive index consequences of the phase change. The K-band radar bright bands occur under light rainfall conditions, presumably due to the dielectric constant effect in relatively small (i.e., Rayleigh scattering) wet snowflakes. The W-band radar V profiles, which are least affected by D^6 sampling effects, support the conclusion that the traditional (S band) radar bright band occurs low in the melting layer near to where many severely melted snowflakes are collapsing into raindrops (as sensed by lidar). This position is close to where the W-band reflectivities and Doppler velocities reach their plateaus, but is well above the height at which the S-band Vs stop increasing. Thus, the radar bright band is dominated by Rayleigh dielectric scattering effects in the few largest melting snowflakes, and is not generally representative of the condition of most of the hydrometeors. The subsequent collapse of these decidedly nonspherical mixed-phase particles into smaller near-spherical drops considerably reduces backscattering with a zenith radar.

As noted first by Lhermitte (1988), W-band radar Z_e often decreases in the upper melting region, or at the least in some of our cases Z_e fails to show the gradual increases seen at longer wavelengths, presumably from the effects of aggregation. This radar dark band was attributed to a Mie backscattering effect in which the mean ice particle size increased enough, perhaps from riming growth just above the 0°C level, to expose the first backscattering minimum in the Mie scattering function. According to Fig. 2, this corresponds to a ~1.0–1.6-mm particle diameter increase for the W-band radar. However, problems with this explanation caused

by the widths of the particle size distribution and other factors were recognized in Lhermitte (2002), and the possibility that an unrepresentative temperature sounding influenced this model should also be considered. We attribute the radar dark band to a combination of Rayleigh and non-Rayleigh scattering effects weighed over the particle size distribution. In particular, while a water-coated snowflake displays increased backscattering in the Rayleigh regime, the opposite is true for larger particles due to the effects of the different refractive indices of water and ice. We can refer to this as the melting hail analogy, which causes non-Rayleigh (χ >~2, or D >~2 mm at λ=0.32 cm) ice spheres to backscatter less energy when water coated than when dry (Fig. 6). The strong backscattering dependence on particle size shown in Fig. 7 indicates that the snowflake size distribution has a large impact on the strength of the W-band radar dark band, explaining why this phenomenon is not consistently observed in the melting layer. Lower in the melting layer, we presume that the shrunken mixed-phase particles are small enough to behave like Rayleigh scatterers and show the usual microwave dielectric effect leading to a gradually increasing Z_e.

Although the concentric water/ice sphere model is a poor representation for melting snowflakes (Di Girolamo et al. 2003), it may apply to conditions in the *initial* melting process. As shown in controlled laboratory ice crystal melting studies (Oraltay and Hallett 1989, 2005), under many environmental conditions meltwater initially coats ice crystal surfaces and then tends to bead up at the intersection of ice branches due to surface tension effects. Heat flow dictates that snowflake melting proceeds from the outermost crystal tips to the center, and as melting progresses, capillary action draws water into the interior of a severely melted particle. Thus, until late in the process, the melting snowflake actually consists of a myriad of water coatings and irregular drop beads. Although it is possible to contrive melting snowflake models that can be applied to Rayleigh scattering to simulate such microscopic melting scenarios (Fabry and Szyrmer 1999), simulating the backscattering of these particles at optical and millimeter wavelengths is confounded by the intricacies of the melting process and the lack of a suitable theoretical approach. Currently, laboratory experiments using lidar and radar analog devices may hold the best promise for increasing our understanding of the scattering processes of the large mixed-phase particles undergoing the phase transition.

In concluding, we emphasize that the exact interrelationships between the various lidar and radar melting-layer features will depend crucially on the precipitation (or attenuation) rate, as well as the size distribution and type of ice particles about to undergo the phase change. Ice particle density and amount of riming will influence the particle fall speeds, and their melting rates. Thus, as indicated here, the details of the bright/dark phenom-

ena can vary noticeably from case to case, and our cases only represent a single geographical region and season.

It is interesting that field research is still disclosing new aspects of the effects of melting-layer microphysics on lidar and radar returns. As stated by Lhermitte (2002), "Even after fifty years of melting-layer observations and studies in various parts of the world, we are still in need of detailed radar observations of reflectivity and Doppler velocity. . .using vertically pointing radars working at different wavelengths from 10 cm to a very short millimeter wave (3.2 mm)." The research reported here represents a step in this direction, which also fortuitously incorporated the special information from the vastly different scattering conditions encountered at the 0.523-μm lidar wavelength.

REFERENCES

Albrecht, B., P. Kollias, R. Lhermitte, and R. Peters, 1999: Observations of tropical cloud systems with a MM-wavelength Doppler radar—An overview. Preprints, *29th Int. Conf. on Radar Meteorology*, Montreal, QC, Canada, Amer. Meteor. Soc., CD-ROM, P3.18.

Battan, L. J., 1973: *Radar Observation of the Atmosphere.* University of Chicago Press, 324 pp.

Bohren, C. F., and D. R. Huffman, 1998: *Absorption and Scattering of Light by Small Particles.* Wiley & Sons, 544 pp.

Campbell, J. R., D. L. Hlavka, E. J. Welton, C. J. Flynn, D. D. Turner, J. D. Spinhirne, V. S. Scott, and I. H. Hwang, 2002: Full-time, eye-safe cloud and aerosol lidar observation at Atmospheric Radiation Measurement Program sites: Instruments and data processing. *J. Atmos. Oceanic Technol.,* **19,** 431–442.

Demoz, B., D. Starr, D. Whiteman, K. Evans, D. Hlavka, and R. Peravali, 2000: Raman lidar detection of cloud base. *Geophys. Res. Lett.,* **27,** 1899–1902.

Dennis, A. S., and W. Hitchfield, 1990: Advances in precipitation physics following the advent of weather radar. *Radar in Meteorology,* D. Atlas, Ed., Amer. Meteor. Soc., 98–108.

Di Girolamo, P., B. B. Demoz, and D. N. Whiteman, 2003: Model simulations of melting hydrometeors: A new bright band from melting frozen drops. *Geophys. Res. Lett.,* **30,** 1626, doi:10.1029/2002GL016825.

Ecklund, W. L., C. R. Williams, P. E. Johnston, and K. S. Gage, 1999: A 3 GHz profiler for precipitating cloud studies. *J. Atmos. Oceanic Technol.,* **16,** 309–322.

Fabry, F., and I. Zawadski, 1995: Long-term radar observations in the melting layer of precipitation and their interpretation. *J. Atmos. Sci.,* **52,** 838–851.

——, and W. Szyrmer, 1999: Modeling of the melting layer. Part II: Electromagnetic. *J. Atmos. Sci.,* **56,** 3593–3600.

Joss, J., and A. Waldvogel, 1990: Precipitation measurement and hydrology. *Radar in Meteorology,* D. Atlas, Ed., Amer. Meteor. Soc., 577–597.

Kerker, M., 1969: *The Scattering of Light and Other Electromagnetic Radiation.* Academic Press, 666 pp.

Lhermitte, R., 1988: Observation of rain at vertical incidence with a 94 GHz Doppler radar: An insight on Mie scattering. *Geophys. Res. Lett.,* **15,** 1125–1128.

——, 2002: *Centimeter and Millimeter Wavelength Radars in Meteorology*. Lhermitte Productions, 550 pp.

Meneghini, R., and L. Liao, 2000: Effective dielectric constants of mixed-phase hydrometeors. *J. Atmos. Oceanic Technol.,* **17,** 628–640.

Michaels, P. J., 1985: Anomalous mid-atmospheric heights and persistent thunderstorm patterns over Florida. *J. Climatol.,* **5,** 529–542.

Mitra, S. K., O. Vohl, M. Ahr, and H. R. Pruppacher, 1990: A wind tunnel and theoretical study of the melting behavior of atmospheric ice particles. VI: Experiment and theory for snow flakes. *J. Atmos. Sci.,* **47,** 584–591.

Moran, K. P., B. E. Martner, M. J. Post, R. A. Kropfli, D. C. Welsh, and K. B. Widener, 1998: An unattended cloud-profiling radar for use in climate research. *Bull. Amer. Meteor. Soc.,* **79,** 443–455.

Oraltay, R. G., and J. Hallett, 1989: Evaporation and melting of ice crystals: A laboratory study. *Atmos. Res.,* **24,** 169–189.

——, and ——, 2005: The melting layer: A laboratory investigation of ice particle melt and evaporation near 0°C. *J. Appl. Meteor.,* **44,** 206–220.

Pruppacher, H. R., and K. Beard, 1970: A wind tunnel investigation of the internal circulation and shape of water drops falling at terminal velocity in air. *Quart. J. Roy. Meteor. Soc.,* **96,** 247–256.

Ro, P. S., T. S. Fahlen, and H. C. Bryant, 1968: Precision measurement of water droplet evaporation rates. *Appl. Opt.,* **7,** 883–890.

Roy, G., and L. R. Bissonnette, 2001: Strong dependence of rain-induced lidar depolarization on the illumination angle: Experimental evidence and geometrical-optics interpretation. *Appl. Opt.,* **40,** 4770–4780.

Sassen, K., 1977a: Lidar observations of high plains thunderstorm precipitation. *J. Atmos. Sci.,* **34,** 1444–1457.

——, 1977b: Optical backscattering from near-spherical water, ice and mixed phase drops. *Appl. Opt.,* **16,** 1332–1341.

——, and T. Chen, 1995: The lidar dark band: An oddity of the radar bright band analogy. *Geophys. Res. Lett.,* **22,** 3505–3508.

——, and L. Liao, 1996: Estimation of cloud content by W-band radar. *J. Appl. Meteor.,* **35,** 932–938.

Simpson, J., C. Kummerow, W. K. Tao, and R. F. Adler, 1996: On the Tropical Rainfall Measuring Mission (TRMM). *Meteor. Atmos. Phys.,* **60,** 19–36.

Spinhirne, J. D., 1993: Micro pulse lidar. *IEEE Trans. Geosci. Remote Sens.,* **31,** 48–55.

Stephens, G. L., and Coauthors, 2002: The CloudSat mission and the A-train: A new dimension of space-based observations of clouds and precipitation. *Bull. Amer. Meteor. Soc.,* **83,** 1771–1790.

Stewart, R. E., J. D. Marwitz, J. C. Pace, and R. E. Carbone, 1984: Characteristics through the melting layer of stratiform clouds. *J. Atmos. Sci.,* **41,** 3227–3237.